ITO@Cu₂S Tunnel Junction Nanowire Arrays as Efficient Counter Electrode for Quantum-Dot-Sensitized Solar Cells

Yan Jiang, Xing Zhang, Qian-Qing Ge, Bin-Bin Yu, Yu-Gang Zou, Wen-Jie Jiang, Wei-Guo Song,* Li-Jun Wan,* and Jin-Song Hu*

CAS Key Laboratory of Molecular Nanostructure and Nanotechnology, Beijing National Laboratory for Molecular Sciences, Institute of Chemistry, Chinese Academy of Sciences (CAS), Beijing 100190, People's Republic of China

S *Supporting Information*

ABSTRACT: Quantum-dot-sensitized solar cell (QDSSC) has been considered as an alternative to new generation photovoltaics, but it still presents very low power conversion efficiency. Besides the continuous effort on improving photoanodes and electrolytes, the focused investigation on charge transfer at interfaces and the rational design for counter electrodes (CEs) are recently receiving much attention. Herein, core−shell nanowire arrays with tin-doped indium oxide (ITO) nanowire core and Cu₂S nanocrystal shell (ITO@Cu₂S) were dedicatedly designed and fabricated as new efficient CEs for QDSSCs in order to improve charge collection and transport and to avoid the intrinsic issue of copper dissolution in popular and most efficient Cu/Cu₂S CEs. The high-quality tunnel junctions formed between n-type ITO nanowires and p-type Cu₂S nanocrystals led to the considerable decrease in sheet resistance and charge transfer resistance and thus facilitated the electron transport during the operation of QDSSCs. The three-dimensional structure of nanowire arrays provided high surface area for more active catalytic sites and easy accessibility for an electrolyte. As a result, the power conversion efficiency of QDSSCs with the designed ITO@Cu₂S CEs increased by 84.5 and 33.5% compared to that with planar Au and Cu₂S CEs, respectively.

KEYWORDS: *Quantum dots, solar cells, nanowires, tunnel junctions, counter electrodes*
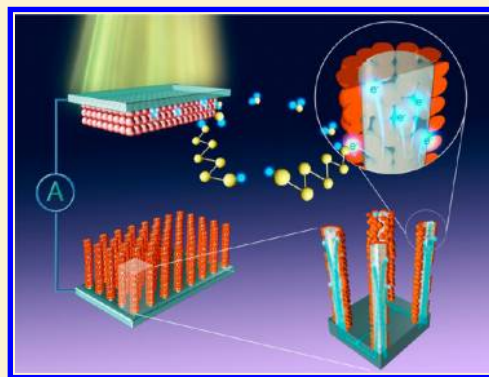
The quantum-dots-sensitized solar cells (QDSSCs) inherit the design of dye-sensitized solar cells (DSSCs) by using quantum dots instead of organic dye as sensitizer.[1−4] Thanks to the high absorption coefficient and quantum confinement effect of quantum dots, QDSSCs have recently received much attention and been considered as an alternative to new generation photovoltaic devices.[5−14] Although the considerable progress has been achieved in recent years, the conversion efficiency of the state-of-the-art QDSSC is still much lower than DSSCs.[15−22] The charge recombination at semiconductor/ electrolyte interface and the poor catalytic activity at counter electrodes (CEs) are considered to be of most importance among possible reasons.[23,24] Nowadays, a noble metal like Pt or Au is widely used as a standard CE because the good interface can be easily achieved between conductive transparent oxide (CTO) and metal catalysts. However, chemisorption of electrolyte (sulfur compounds) on Pt or Au causes a high overpotential and thus inefficient reduction of redox polysulfide, so that the device presents a rather low fill factor and power conversion efficiency.[25] Metal-chalcogenides, such as Cu₂S,[26−28] PbS,[29,30] CoS,[31] and copper zinc tin sulfide,[32,33] have been reported as effective CE materials due to their much higher electrocatalytic activity in reducing Sₙ²⁻ to nS²⁻. Copper foil-based CEs exhibit excellent performance but suffer from mechanical instability while the reaction between copper and electrolyte makes the situation unclear.[27,29] Presynthesized

semiconductor nanocrystals have been also attempted to fabricate CEs in combination with conductive materials like graphene and carbon black to compensate their insufficient electron conductivity.[29] These materials usually impart CEs small charge transfer resistance (R_{ct}) but somewhat large sheet resistance (R_h). The effort to further decrease R_h has witnessed the improvement of device performance. For example, introducing polyvinylidene fluoride into Cu₂S/reduced graphene oxide (RGO) composite CE as a binder decreased its R_h, which resulted in the increase in conversion efficiency of QDSSC.[27] Therefore, the rationally designed CEs for the purpose of reducing R_{ct} and R_h, as well as improving semiconductor−electrode interface would be highly desirable and significant to further enhance the power conversion efficiency of QDSSCs.

Herein, tunnel junction arrays configured with degenerate n-type tin-doped indium oxide nanowire (ITO) core and degenerate p-type Cu₂S nanocrystal shell (designated as ITO@Cu₂S) were designed and fabricated as new efficient CE for QDSSCs. ITO nanowire array core provided a three-dimensional conductive network. ITO core and Cu₂S nanocrystal shell formed effective tunnel junctions with carrier
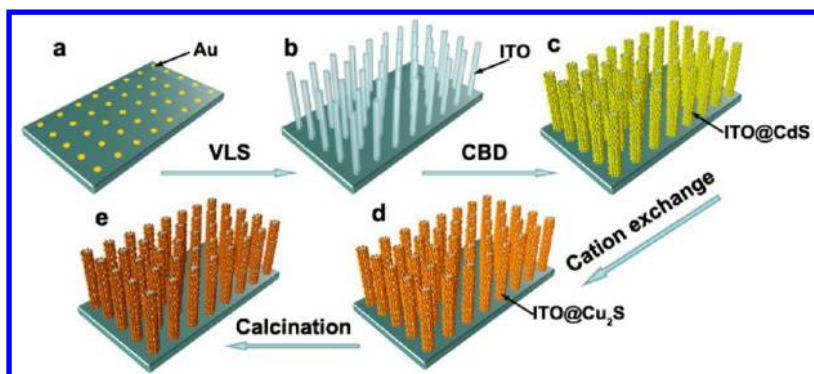
Figure 1. Scheme for directly preparing ITO@Cu$_2$S nanowire arrays on FTO glass. (a) Sputtering Au catalysts on FTO substrate; (b) CVD synthesis of ITO nanowire arrays; (c) chemical bath deposition of CdS shell on ITO nanowire arrays; (d) cation exchange to form ITO@Cu$_2$S nanowire arrays; (e) calcination for improving the interfaces between ITO nanowire core and Cu$_2$S nanocrystal shell.
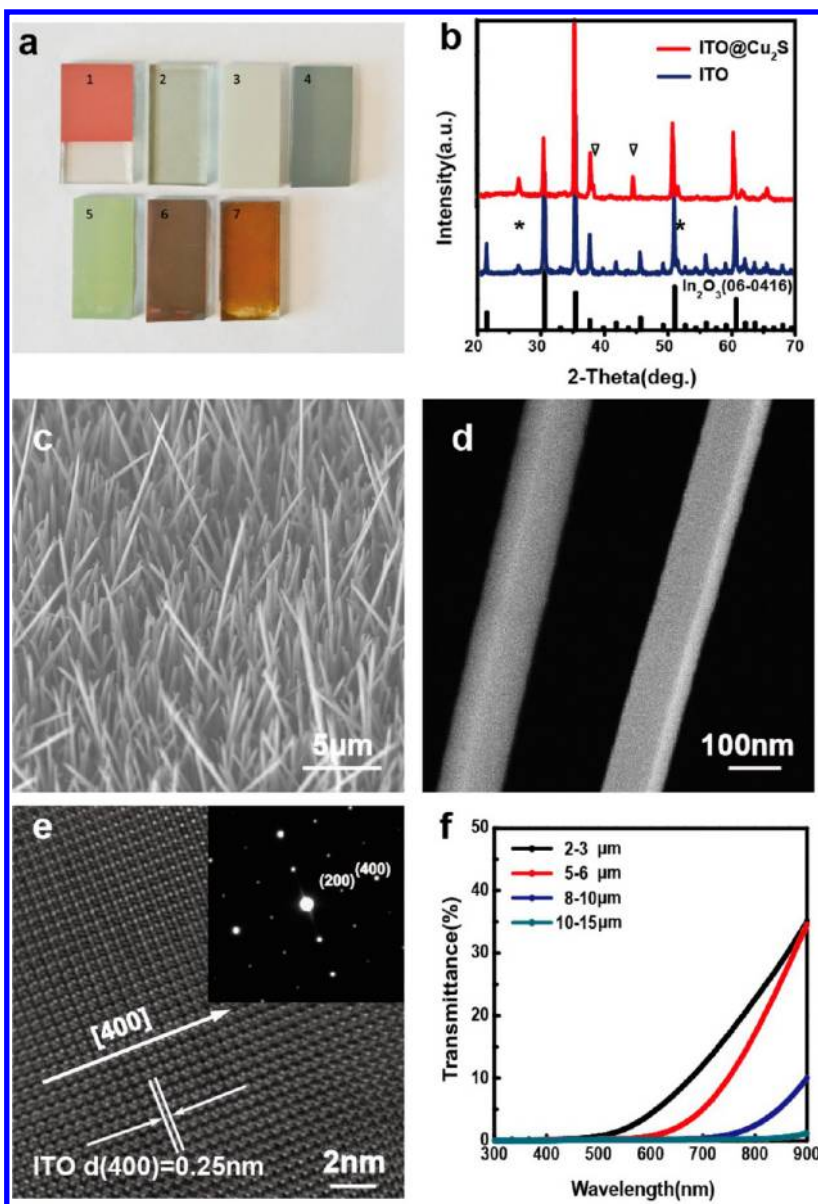

Figure 2. (a) Optical images of CdS/CdSe quantum dot cosensitized TiO$_2$ film (a$_1$), Au CE (a$_2$), ITO nanowire arrays (a$_3$), ITO@Au nanowire arrays (a$_4$), ITO@CdS nanowire arrays (a$_5$), ITO@Cu$_2$S nanowire arrays (a$_6$), and Cu$_2$S CE (a$_7$). (b) XRD patterns of ITO (blue), ITO@Cu$_2$S (red), and the reference In$_2$O$_3$ (JCPDS Card No. 06-0416). (c) Typical low-magnification SEM image and (d) high-magnification SEM image of ITO nanowires. (e) Typical TEM image of ITO nanowire. The inset is SAED pattern. (f) Transmittance of ITO nanowire arrays in different lengths.

transport path shorter than 100 nm. It was found that R_h was not only dependent on the electron conductivity of the substrate but also related to the semiconductor–electrode interface between CTO and catalysts. The high-quality tunnel junctions resulted in the considerable decrease in R_h and facilitated electron transfer from CTO to Cu_2S. Moreover, the chemically inert nature of ITO made CE stable in liquid electrolyte with no intrinsic issue like copper dissolution in state-of-the-art Cu/Cu_2S CE. Compared with planar structures, the three-dimensional structure of nanowire arrays presented higher surface area for loading more catalysts and easy accessibility of electrolyte, leading to the enhancement of the catalytic activity of CEs as evidenced by apparently decreased R_{ct}. As a result, the power conversion efficiency of QDSSCs with the designed ITO@Cu_2S nanowire CEs increased by 84.5 and 33.5% compared to that with Au and Cu_2S CEs, respectively.

Results and Discussion. As shown in Figure 1, ITO@Cu_2S nanowire array CE was fabricated by coating single-crystalline ITO nanowire array on FTO substrate with Cu_2S nanocrystal shell. In brief, single-crystalline ITO nanowire arrays were first grown on Au-coated FTO substrate via chemical vapor deposition (CVD). Metallic indium and tin powders were used as source materials and an air flow for reactive atmosphere. In order to prepare ITO@Cu_2S nanowire arrays with high-quality ITO/Cu_2S tunnel junctions, the as-prepared ITO nanowires were first coated with a layer of CdS in a thickness of about 20 nm via chemical bath deposition (CBD) technique. After that, a solution-based cation exchange was carried out to achieve ITO@Cu_2S coaxial nanowire arrays, followed by calcination to improve the interfaces between ITO nanowires and Cu_2S nanocrystals.

As seen in optical images of products at different stages (Figure 2a), the FTO substrate was covered with white-gray film after CVD growth (sample 3). The composition and structure of the film was characterized by X-ray diffraction (XRD) experiments. As presented in Figure 2b (blue line), the diffraction peaks of the film can be well indexed to cubic In_2O_3 (JCPDS Card No. 06-0416, black pattern) except for two peaks (marked as star) at 26.6 and 51.8°, which can be attributed to the diffraction on (100) and (211) crystallographic planes of SnO_2 (JCPDS Card No. 41-1445), respectively. The result indicates the white-gray film is composed of tin-doped indium oxide.[34] The sharp shape of diffraction peaks implies that the prepared ITO film is well crystallized.

The morphology of the film was investigated by scanning electron microscopy (SEM). Figure 2c presents a typical low-magnification SEM image of the ITO film. It is clearly seen that the film comprises of a great amount of nanowires vertically grown on the substrate. The diameters of these nanowires are in a range of around 100–120 nm. The faceted shape and smooth side surfaces indicate the nanowires have good crystallinity, as shown in the typical high-magnification SEM image (Figure 2d). Moreover, the length of ITO nanowires can be easily tuned by changing the distance between the substrate and the sources and the growth time during CVD growth. For example, ITO nanowires in average lengths from 2 to 15 μm were obtained and used in this study. The SEM images of the ITO nanowires with different lengths are presented in Figure S1 in Supporting Information. The crystal structure and growth direction of ITO nanowire were further investigated by high-resolution transmission electron microscopy (HRTEM). Figure 2e shows clear and continuous lattice fringes, revealing the

single-crystalline nature and good crystallinity of the nanowire. The lattice spacing of 0.25 nm matches well with the interplanar spacing (400) planes of cubic In_2O_3, indicating the nanowire grows along [400] crystallographic direction based on the fact that these lattice fringes are perpendicular to the length direction of nanowire. The selected area electron diffraction (SAED) pattern in inset of Figure 2e corroborates this result.

The light transmittance is one of important parameters for CEs. The low light transmittance would be preferable for allowing efficient light absorption. As shown in Figure 2f, the light transmittance of ITO nanowire film decreases as the increase in the length of the nanowires. The longer the nanowires are, the less light will pass through the nanowire film, indicating that more light will be scattered or reflected on counter electrode. For example, when the length of ITO nanowire reaches about 8–10 μm, the light transmittance is less than 1% in the visible light region.

After CBD and cation exchange process (Figure 1c–e), the dark-brown film on substrate (sample 6 in Figure 2a) was calcinated and then characterized by XRD to reveal its composition and structure. Two more peaks were found in the recorded XRD pattern (red pattern in Figure 2b) at 38.5 and 44.8° compared to pure ITO nanowire array film (blue pattern in Figure 2b), which can be well attributed to the diffraction from (240) and (204) crystallographic planes of low-chalcocite Cu_2S. It should be noted that no additional peaks were observed in the pattern, implying CdS shell was completely converted into Cu_2S after cation exchange. The SEM image of the product shows that the ITO nanowires were coaxially coated with a shell of nanoparticles (Figure 3a,b). The elemental analysis via energy dispersive X-ray spectroscopy (EDS) equipped on SEM (Figure S2 in Supporting Information) shows that these nanowires are composed of
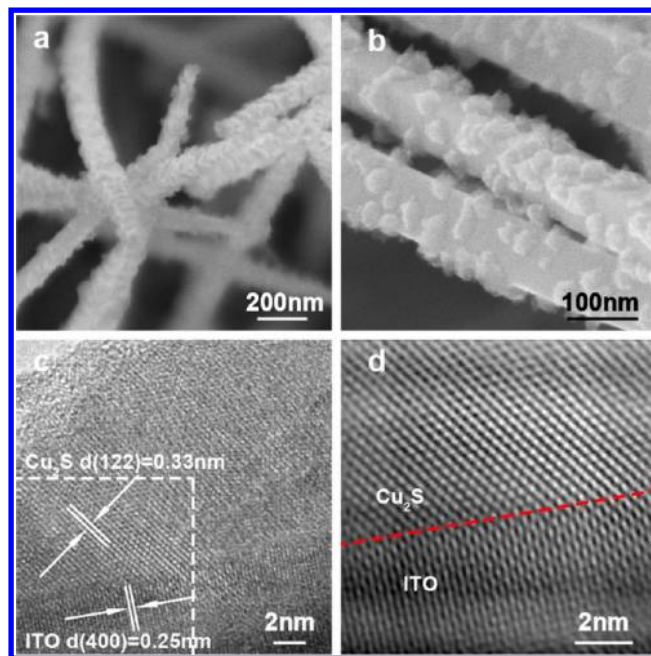

Figure 3. (a) Low-magnification and (b) high-magnification SEM images of ITO@Cu_2S. (c) HRTEM image showing the interface of Cu_2S nanocrystal shell and ITO nanowire core. (d) Constructed inverse FFT image of the area squared in panel c. The red line marked the intimate and defect-free interface.
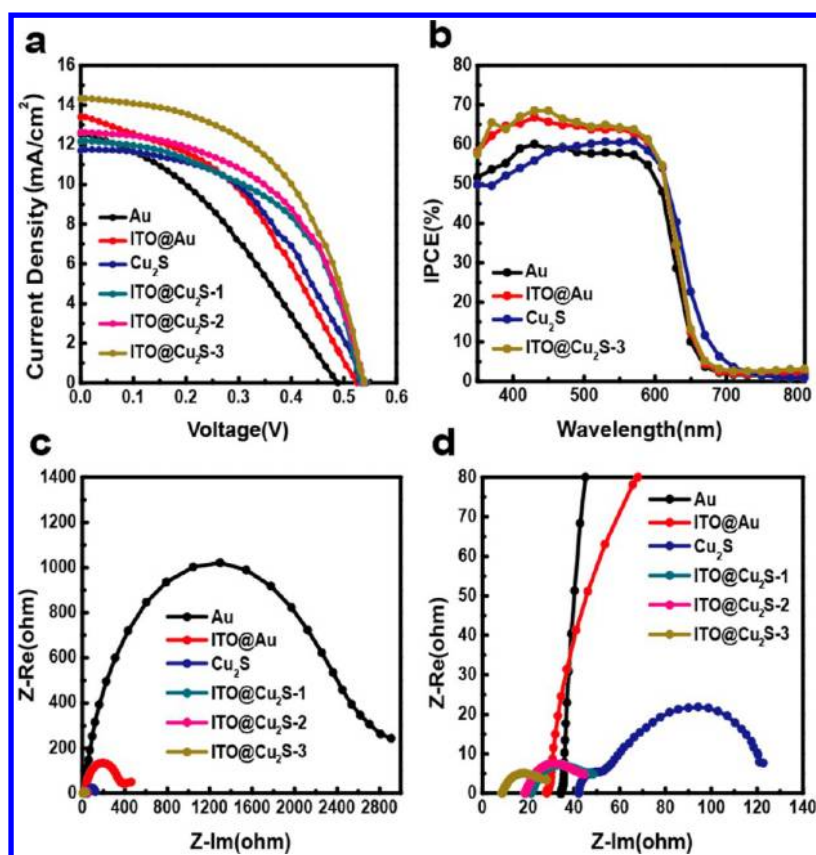
Figure 4. (a) Photocurrent−voltage (*J*−*V*) curves and (b) IPCE spectra of QDSSCs with different CEs. ITO@Cu$_2$S-1, -2, and -3 represent that ITO nanowires are 2−3 μm, 5−6 μm, and 8−10 μm long, respectively. (c) Nyquist plots from the impedance measurement of different CEs. (d) Zoom-in view of panel c in the high-frequency region.

Table 1. Photovoltaic Parameters of QDSSCs with Different CEs

CEs	V_{oc} (V)	J_{sc} (mA cm^{-2})	FF (%)	η (%)	R_h (Ω)	R_{ct1} (Ω cm^2)	R_{ct2} (Ω cm^2)
Au	0.488	12.54	35.92	2.20	17.94	[a]	437.58
ITO@Au	0.525	13.39	41.74	2.94	15.97	[a]	58.63
Cu$_2$S	0.543	11.70	47.76	3.04	21.71	2.77	8.48
ITO@Cu$_2$S-1	0.533	12.16	51.93	3.37	11.08	[a]	3.73
ITO@Cu$_2$S-2	0.538	12.61	52.12	3.54	9.34	[a]	3.68
ITO@Cu$_2$S-3	0.540	14.31	52.48	4.06	4.66	[a]	2.64

[a]No R_{ct1} can be detected.

elements In, Sn, O, as well as Cu and S. No element Cd was detected. Figure 3c presents a typical HRTEM image of ITO@Cu$_2$S nanowire. Clear crystal lattice fringes in whole imaging region demonstrate that both core and shell of nanowire are well crystallized. The distance of lattice fringes in shell part (0.33 nm) is consistent with the interplanar spacing (122) planes of low-chalcocite Cu$_2$S, suggesting the shell part is Cu$_2$S nanocrystal. The EDS mapping analysis confirms that the nanowire is composed of ITO core and Cu$_2$S nanocrystal shell (Supporting Information Figure S3). In order to clearly reveal the interface between core and shell, the marked square region in Figure 3c was reconstructed to an inverse FFT image (Figure 3d). It is interesting to note that the lattice fringes of Cu$_2$S nanocrystals linked smoothly with that of ITO nanowire core with no obvious defects, which indicates the Cu$_2$S nanocrystal epitaxially grew on the ITO core. It was proved hereinafter that this intimate and defect-free contact guaranteed the formation of high quality ITO/Cu$_2$S tunnel junctions which facilitated charge transfer and contributed to the decrease of R_h.

The junction was further investigated by determining the doping levels of ITO and Cu$_2$S. Ultraviolet photoelectron spectroscopy (UPS) experiment was carried out to determine the valence band maximum (VBM) of ITO nanowire array (See Supporting Information for details, Figure S4). The result shows the Femi level (E_f) of the prepared ITO nanowire array is ca. 0.12 eV beyond the conductive band minimum (CBM), which means it is an n-type degenerate semiconductor. Because the similar analysis cannot be reliably applied on ITO@Cu$_2$S nanowire due to the discontinuity of Cu$_2$S nanocrystal shell, the Hall measurement was done on Cu$_2$S thin film that was grown on glass slide in parallel with the preparation of ITO@Cu$_2$S nanowire (see Supporting Information for details). The hole carrier density was measured to be 2.39×10^{20} cm^{-3} (Supporting Information Table S2), indicating that the as-prepared Cu$_2$S is p-type degenerate semiconductor.[35] As a result, ITO and Cu$_2$S could form effective tunnel junction when ITO@Cu$_2$S nanowires were used as CEs of QDSSCs. This could be further corroborated by the fact that the sheet
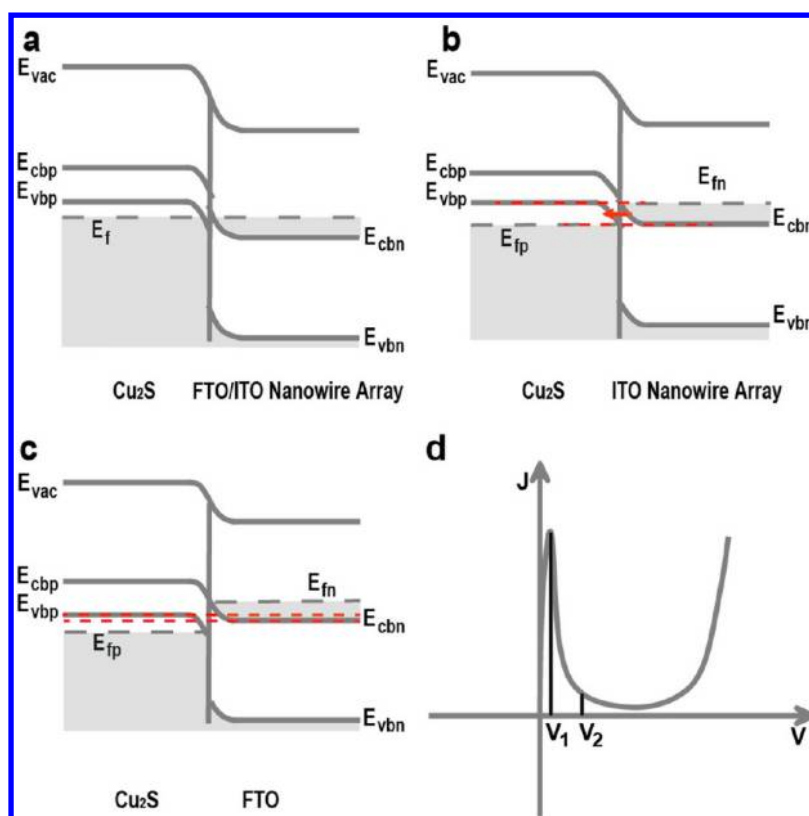
Figure 5. Schematic band diagrams. (a) Junction of Cu_2S and FTO or ITO nanowire arrays when QDSSC is off work. (b) Junction of Cu_2S and ITO nanowire arrays, and (c) junction of Cu_2S and FTO when QDSSC is at work. (d) Typical IV characteristic of a tunnel junction. The formation of tunnel junction between ITO nanowire and Cu_2S nanocrystal enlarges the amount of quantum states at same energy across the junction (region marked with red dashed lines in panels b and c) and thus facilitates electron tunneling and greatly reduces R_h.

resistances of the nanowire CEs decreased from 4.0 $\Omega/\square$ for pure ITO nanowires on FTO substrate to 2.9 $\Omega/\square$ after incorporating Cu_2S nanocrystal shell, and further to 2.1 $\Omega/\square$ after annealing (Supporting Information Table S3). The formation of the tunnel junction would facilitate the electron transfer from ITO to Cu_2S.[36]

The ITO@Cu_2S nanowires with three different lengths were used as CEs to fabricate QDSSCs for evaluating their performance. For comparison, Au-sputtered FTO, Au-sputtered ITO nanowire, and Cu_2S coated FTO were also used as CEs to fabricate reference QDSSCs in parallel and designated as Au, ITO@Au, and Cu_2S CE, respectively. The details for the fabrication of each CE were presented in the Experimental Section. Figure 4a shows the $J-V$ curves of the QDSSCs with different CEs. The device parameters are summarized in Table 1. Compared to the device with traditional Au CE, the device with ITO@Au nanowire CE exhibited both higher V_{oc} (0.525 V vs 0.488 V) and higher fill factor (FF) (41.74% vs 35.92%) since three-dimensional structure of ITO nanowire arrays provided more catalytic sites. The V_{oc} and FF of the device with Cu_2S CE are greater than that of devices with Au or ITO@Au nanowire CEs due to the higher catalytic activity of Cu_2S nanocrystals than Au in this system. It is also interesting to note that the short-circuit photocurrent density (J_{sc}) and FF of the devices were much enhanced after integrating Cu_2S nanocrystals onto ITO nanowires. Specifically speaking, the J_{sc} and FF of the device with 8−10 μm long ITO@Cu_2S nanowire CE increased by 14.1 and 46.1% compared to the device with Au CE and 22.3 and 9.9% compared to the device with Cu_2S CE, respectively. As a result, the power conversion efficiency of

QDSSCs with the ITO@Cu_2S CE increased by 84.5 and 33.5% compared to that with Au and Cu_2S CEs, respectively. The device performance was related to the length of ITO nanowire and enhanced as the increase in length of ITO nanowire, which also indicates that this improvement is truly from the designed structure of ITO@Cu_2S nanowire. Figure 4b shows the incident photon-to-electron conversion efficiency (IPCE) spectra of typical QDSSCs based on four different CEs, including Au, ITO@Au, Cu_2S, and ITO@Cu_2S-3. The obvious drop of IPCE at around 630 nm corresponds to the absorption edge of CdSe quantum dots. A comparison of the IPCE spectra reveals ~8% increase was achieved after introducing ITO nanowire arrays for both Au- and Cu_2S-based CEs, which is in good agreement with the increase in J_{sc}.

In order to understand the reason for the improvement of device performance, the electrochemical impedance spectroscopy (EIS) experiments were carried out on each kind of CEs by using the symmetrical cells with two CEs sandwiching electrolyte. The measurement was operated at zero potential bias with AC amplitude of 10 mV and a frequency range between 100 mHz to 100 kHz. Figure 4c shows the EIS spectra and Figure 4d is a zoom-in view of Figure 4c in the high-frequency region. The suitable equivalent circuits were modeled as shown in Supporting Information Figure S5 and the resulting parameters were summarized in Table 1. In the case of Au-based CEs, because the nanowire arrays presented much a higher surface area to load more catalysts compared with the planar structure, the charge transfer resistance at the interface of CE and the electrolyte (R_{ct2}) decreased strikingly after introducing ITO nanowire arrays (58.63 Ω cm^2 vs 437.58 Ω

cm^2), indicating the enhancement of the catalytic activity. As a result, the FF of the devices increased from 35.92 to 41.74%, and V_{oc} increased from 0.488 to 0.525 V by introducing ITO nanowire array. As ITO is an n-type degenerate semiconductor, an ohmic contact could be achieved in ITO@Au CE via metal-n+ contact. No obvious R_{ct1} was found in EIS measurement. Moreover, as seen in Table 1, a much smaller R_{ct2} was achieved (8.48 Ω cm^2 vs 437.58 Ω cm^2) in Cu$_2$S CE compared with that in Au CE. R_{ct2} was further reduced by incorporating Cu$_2$S on ITO nanowire arrays. The smallest R_{ct2} of 2.64 Ω cm^2 was obtained on 10 μm long ITO@Cu$_2$S nanowire. According to the above analysis, the small R_{ct2} implied that the device with Cu$_2$S-based CE would show a higher FF and V_{oc} than that with Au-based CE, which is consistent with the data shown in Table 1. On the other hand, it can be seen that R_h of ITO@Cu$_2$S-1 CE was about two times smaller than that with Cu$_2$S CE (11.08 Ω vs 21.71 Ω) and further decreased as the increase in length of ITO nanowires (4.66 Ω for ITO@Cu$_2$S-3 CE). J_{sc}, FF, and power conversion efficiency were subsequently increased as the decrease in R_h.

As mentioned above, tunnel junction formed in Cu$_2$S-based CE and contributed to the decrease in sheet resistance. The schematic band diagrams of different junctions are depicted in Figure 5 to further understand the influence of tunnel junction in this system on R_h. Figure 5a,b shows the schematic band diagram of tunnel junction in ITO@Cu$_2$S CE when QDSSC is off or at work, respectively. When QDSSC is at work, a forward potential exists across the junction, leading to the upward shift of Femi level of FTO (E_{fn}). The formation of tunnel junction allows the existence of quantum states with same energy level on both sides of the junction as the upward shift of E_{fn}. Consequently, the electrons in the quantum states between E_{fn} and conduction band (E_{cbn}) at ITO side will tunnel through to the empty quantum states at same energy level between valence band (E_{vbp}) and E_{fp} at Cu$_2$S side and generate tunnel current. Figure 5d depicts a typical $I-V$ curve of tunnel junction. Given that the resistance of Cu$_2$S-based CE in the present study is much smaller than that of photoanode, the forward potential should be in the region of negative differential resistance in Figure 5d. On the basis of EIS results, the charge transfer resistance between FTO and Cu$_2$S (R_{ct1}) was observed in Cu$_2$S electrode (as manifested by the semicircle in high frequency in Nyquist plot of Figure 4d), while no obvious R_{ct1} exists in ITO@Cu$_2$S electrodes. This resistance will lead to a forward potential at the junction, so that the forward potential across the junction in Cu$_2$S electrode is larger than that in ITO@Cu$_2$S electrode (schematically shown as V_2 and V_1 in Figure 5d, respectively). Since the shift of Femi level decreases as the decrease in potential, the amount of quantum states at same energy level across the junction in ITO@Cu$_2$S electrode will be larger than that in Cu$_2$S CE (region marked with red dashed lines in Figure 5b and 5c), and reach the maxima when the bottom of ITO E_{cbn} is approaching the Femi level of Cu$_2$S (E_{fp}), which will augment the probability of electron tunneling to generate tunnel current. This result is consistent with the remarkable decrease in R_h. It should be noted that R_h was generally considered to be dependent on the conductivity of the electrode.[29] Here, we have shown that R_h is also closely relevant to R_{ct1}. In a common QDSSC, the series resistance (R_s) can be defined as

$$R_s = R_h + R_{ct1} + R_{ct2} + R_w \tag{1}$$

wherein R_w is designated as Warburg diffusion impedance within the electrolyte. Because the same electrolyte was used in each system, R_w should be almost the same. R_s is basically dependent on the sum of R_h, R_{ct1}, and R_{ct2}. Because the designed ITO@Cu$_2$S nanowire array in the present study exhibited both smaller R_h and R_{ct}, the devices with them as CEs would have smaller R_s. Therefore, the devices displayed the enhanced J_{sc}, FF, and power conversion efficiency. This improvement can be further enhanced by using longer ITO nanowire. For example, the cell with 10 μm ITO@Cu$_2$S nanowire array as CE has shown an increase of 84.5 and 33.5% in power conversion efficiency compared to that with pure Au and Cu$_2$S CEs, respectively.

Conclusion. In conclusion, a coaxial nanowire array with single crystalline ITO nanowire as core and Cu$_2$S nanocrystal as sheath was successfully designed and fabricated as new efficient CE for QDSSC. The formation of high-quality tunnel junctions with short carrier transport path (less than 100 nm) between core and sheath significantly reduced the sheet resistance of CE and facilitated electron transfer from CTO to Cu$_2$S. The three-dimensional structure of nanowire array provided more active catalytic sites and easy accessibility for electrolyte, which led to the remarkable decrease in charge transfer resistance and the enhancement of catalytic activity of CE. As a result, the QDSSC with the designed ITO@Cu$_2$S nanowire CE demonstrated an increase of 84.5 and 33.5% in power conversion efficiency compared to that with planar Au and Cu$_2$S CEs, respectively. It is believed that the power conversion efficiency can be further enhanced by optimizing the coverage and size of Cu$_2$S nanocrystals on ITO nanowire array, the length and density of ITO nanowire array, as well as the material and structure of photoanode. The design ideas reported here could be adapted to design other efficient counter electrodes for not only QDSSCs but DSSCs.

Experimental Section. *Synthesis of ITO nanowire arrays.* FTO substrates (14 $\Omega/\square$, Nippon Sheet Glass) were cleaned by sequentially sonicating in water, ethanol, and acetone thoroughly, followed by O$_2$ plasma cleaning. Gold nanoparticles were sputtered on FTO as catalysts via a sputtering coater (JFC-1600 Auto Fine Coater, JEOL). High-purity (99.99%) metallic indium and tin powders were used as source in a weight ratio of 10:1 to grow ITO nanowire arrays at a source temperature of 800 °C, a pressure of 30 Pa and an air flow of about 1.5 sccm. The white gray products were obtained after growth. The average length of ITO nanowires is dependent on the distance from substrate to the source as well as the growth time.

Synthesis of ITO@Cu$_2$S nanowire arrays. In order to coaxially grow Cu$_2$S nanocrystals on ITO nanowire cores, chemical bath deposition (CBD) technique was used to first grow about 20 nm thick CdS shell. Typically, FTO with ITO nanowire arrays was immersed into a solution containing 20 mM CdCl$_2$, 66 mM NH$_4$Cl, and 140 mM thiourea at 25 °C. The yellowish product was obtained after 2 h and then was washed thoroughly with DI water. A solution-based cation exchange was subsequently carried out to convert CdS into Cu$_2$S. In a typical process, the as-synthesized ITO@CdS coaxial nanowire arrays were immersed into 0.5 M CuCl aqueous solution at 50 °C for 5 min. The color of the substrate was immediately changed from light yellow to dark brown. The product was washed thoroughly with DI water, dried, and then calcined at 400 °C for 30 min in Ar atmosphere.

Characterization. The morphology and composition of as-prepared ITO and ITO@Cu₂S nanowire arrays were characterized by FE-SEM (JSM 6701, JEOL) equipped with energy dispersive X-ray spectroscopy detector (Oxford) and TEM (JEM 2100F, JEOL). The XRD experiments were carried out on a Rigaku D/max-2500 diffractometer. Transmittance was measured with a UV−vis spectrophotometer (SHIMAD-ZU) UV-2550 in a transmittance mode. Ultraviolet photoelectron spectra were taken on an ESCALAB250XI X-ray photoelectron spectroscope. Hall Effect measurement was done on Ecopia HMS-3000. Film thickness was tested on a Dektak XT Profilometer. Electrochemical impedance spectroscopy was carried out on a PARSTAT 2273A potentiostat.

Preparation of photoanodes. CdS/CdSe sensitized TiO_2 photoanodes were prepared according to literature except that commercial P25 TiO_2 nanoparticles (Degussa) were used instead.[16] In brief, P25 nanoparticles were dispersed in 1-butanol to form a paste by sonicating and stirring overnight. Five wt % triton was introduced to reduce evaporation rate. The paste was coated on clean FTO substrate to obtain TiO_2 porous film via a doctor blade method. The substrate was then treated with $TiCl_4$ and calcinated to enhance the connection among TiO_2 nanoparticles. After that, the film was sensitized with CdS and CdSe quantum dots and passivated with ZnS. The thickness of the film is about 10.55 μm based on SEM image (Supporting Information Figure S6).

Preparation of Counter Electrodes. ITO@Cu₂S nanowire arrays in different lengths were used as counter electrodes and designated as ITO@Cu₂S-1, ITO@Cu₂S-2, and ITO@Cu₂S-3 for 2−3 μm, 5−6 μm, and 8−10 μm long ITO nanowires, respectively. Au, ITO@Au nanowire array, and Cu₂S-coated FTO were used as reference CEs. Au and ITO@Au CEs were prepared by sputtering about 8 nm thick Au nanoparticles on FTO without or with 8−10 μm long ITO nanowires, respectively. Cu₂S CE was prepared in parallel with with the preparation of ITO@Cu₂S CEs except for using pure FTO instead of FTO with ITO nanowires.

Preparation of QDSSCs. QDSSCs were fabricated by encapsulating the polysulfide electrolyte consisting of 1 M S,1 M Na_2S, and 0.2 M KCl in water/methanol (3:7, v/v) solution between the photoanode and the each above-mentioned CEs with 3 M adhesive tape in a thickness of about 50 μm as spacer. A copper mask with a window of 0.16 cm² was clipped on the photoanode to define the active area of the cell.

Photovoltaic Measurements. For I−V test, a sandwiched QDSSC was irradiated by a solar simulator (450W Model 91150, Newport) with an AM 1.5 spectrum distribution calibrated against a NREL reference cell to accurately simulate one full-sun intensity (100 mW/cm²). IQE-200 measurement system with a motorized 1/8 m monochromator (model 74000, Newport) in DC mode was used for all IPCE tests.

ASSOCIATED CONTENT

ⓢ Supporting Information

SEM images of ITO nanowire arrays in different lengths, EDS spectrum taken on as-synthesized ITO@Cu₂S, the elemental mapping results of a ITO@Cu₂S nanowire, UPS spectrum of ITO nanowire array, Hall Effect measurement of Cu₂S film, sheet resistance measurement of ITO and ITO@Cu₂S before and after calcination, cross-sectional SEM image of TiO_2 photoanode, TEM image of the CdS/CdSe cosensitized TiO_2 photoanode, and equivalent circuits for fitting EIS of different CEs. This material is available free of charge via the Internet at http://pubs.acs.org.

AUTHOR INFORMATION

Corresponding Authors
*E-mail: (J.-S.H.) hujs@iccas.ac.cn.
*E-mail: (W.-G.S.) wsong@iccas.ac.cn.
*E-mail: (L.J.W.) wanlijun@iccas.ac.cn.
Notes
The authors declare no competing financial interest.

ACKNOWLEDGMENTS

REFERENCES

(1) Nozik, A. J.; Miller, J. R. *Chem. Rev.* **2010**, *110*, 6443−6445.
(2) Chen, G.; Seo, J.; Yang, C.; Prasad, P. *Chem. Soc. Rev.* **2013**, 8304−8338.
(3) Graetzel, M.; Janssen, R. A.; Mitzi, D. B.; Sargent, E. H. *Nature* **2012**, *488*, 304−312.
(4) Ruhle, S.; Shalom, M.; Zaban, A. *ChemPhysChem* **2010**, *11*, 2290−2304.
(5) Tang, J.; Sargent, E. H. *Adv. Mater.* **2011**, *23*, 12−29.
(6) Smith, A. M.; Nie, S. *Acc. Chem. Res.* **2010**, *43*, 190−200.
(7) Wise, F. W. *Acc. Chem. Res.* **2000**, *33*, 773−780.
(8) Sukhovatkin, V.; Hinds, S.; Brzozowski, L.; Sargent, E. H. *Science* **2009**, *324*, 1542−1544.
(9) Sambur, J. B.; Novet, T.; Parkinson, B. A. *Science* **2010**, *330*, 63−66.
(10) Semonin, O. E.; Luther, J. M.; Choi, S.; Chen, H. Y.; Gao, J.; Nozik, A. J.; Beard, M. C. *Science* **2011**, *334*, 1530−1533.
(11) Nozik, A. J. *Nat. Photonics* **2012**, *6*, 272−273.
(12) Burschka, J.; Pellet, N.; Moon, S. J.; Humphry-Baker, R.; Gao, P.; Nazeeruddin, M. K.; Gratzel, M. *Nature* **2013**, 316−319.
(13) Lee, M. M.; Teuscher, J.; Miyasaka, T.; Murakami, T. N.; Snaith, H. J. *Science* **2012**, *338*, 643−647.
(14) Zhuang, Z.; Peng, Q.; Wang, X.; Li, Y. *Angew. Chem., Int. Ed.* **2007**, *46*, 8174−8177.
(15) Yu, X.; Liao, J.; Qiu, K.; Kuang, D.; Su, C. *ACS Nano* **2011**, *5*, 9494−9500.
(16) Zhang, Q.; Guo, X.; Huang, X.; Huang, S.; Li, D.; Luo, Y.; Shen, Q.; Toyoda, T.; Meng, Q. *Phys. Chem. Chem. Phys.* **2011**, *13*, 4659−4667.
(17) Nattestad, A.; Mozer, A. J.; Bach, U. *Nat. Mater.* **2009**, *9*, 31−35.
(18) Yella, A.; Lee, H. W.; Tsao, H. N.; Yi, C.; Chandiran, A. K.; Nazeeruddin, M. K.; Diau, E. W.; Yeh, C. Y.; Zakeeruddin, S. M.; Gratzel, M. *Science* **2011**, *334*, 629−634.
(19) Santra, P. K.; Kamat, P. V. *J. Am. Chem. Soc.* **2013**, *135*, 877−885.
(20) Lee, J. W.; Son, D. Y.; Ahn, T. K.; Shin, H. W.; Kim, I. Y.; Hwang, S. J.; Ko, M. J.; Sul, S.; Han, H.; Park, N. G. *Sci. Rep.* **2013**, *3*, 1050.
(21) Yan, K.; Zhang, L.; Qiu, J.; Qiu, Y.; Zhu, Z.; Wang, J.; Yang, S. *J. Am. Chem. Soc.* **2013**, *135*, 9531−9539.
(22) Qian, J.; Jiang, K. J.; Huang, J. H.; Liu, Q. S.; Yang, L. M.; Song, Y. *Angew. Chem., Int. Ed.* **2012**, *51*, 10351−10354.
(23) Hou, Y.; Wang, D.; Yang, X. H.; Fang, W. Q.; Zhang, B.; Wang, H. F.; Lu, G. Z.; Hu, P.; Zhao, H. J.; Yang, H. G. *Nat. Commun.* **2013**, *4*, 1583.
(24) Kamat, P. V. *Acc. Chem. Res.* **2012**, *45*, 1906−1915.

(25) Yang, Y. C.; Lee, Y. L. *J. Am. Chem. Soc.* **2006**, *128*, 3677−3682.

(26) Gimenez, S.; Mora-Sero, I.; Macor, L.; Guijarro, N.; Lana-Villarreal, T.; Gomez, R.; Diguna, L. J.; Shen, Q.; Toyoda, T.; Bisquert, J. *Nanotechnology* **2009**, *20*, 295204.

(27) Radich, J. G.; Dwyer, R.; Kamat, P. V. *J. Phys. Chem. Lett.* **2011**, *2*, 2453−2460.

(28) Chen, H.; Zhu, L.; Liu, H.; Li, W. *J. Phys. Chem. C* **2013**, *117*, 3739−3746.

(29) Yang, Y.; Zhu, L.; Sun, H.; Huang, X.; Luo, Y.; Li, D.; Meng, Q. *ACS Appl. Mater. Interfaces* **2012**, *4*, 6162−6168.

(30) Tachan, Z.; Shalom, M.; Hod, I.; Rühle, S.; Tirosh, S.; Zaban, A. *J. Phys. Chem. C* **2011**, *115*, 6162−6166.

(31) Yang, Z.; Chen, C.-Y.; Liu, C.-W.; Li, C.-L.; Chang, H.-T. *Adv. Energy Mater.* **2011**, *1*, 259−264.

(32) Xin, X.; He, M.; Han, W.; Jung, J.; Lin, Z. *Angew. Chem., Int. Ed.* **2011**, *50*, 11739−11742.

(33) Zeng, X.; Zhang, W.; Xie, Y.; Xiong, D.; Chen, W.; Xu, X.; Wang, M.; Cheng, Y.-B. *J. Power Sources* **2013**, *226*, 359−362.

(34) Noh, J. H.; Han, H. S.; Lee, S.; Kim, J. Y.; Hong, K. S.; Han, G.-S.; Shin, H.; Jung, H. S. *Adv. Energy Mater.* **2011**, *1*, 829−835.

(35) Page, M.; Niitsoo, O.; Itzhaik, Y.; Cahen, D.; Hodes, G. *Energy Environ. Sci.* **2009**, *2*, 220−223.

(36) Jeon, S.-R.; Song, Y.-H.; Jang, H.-J.; Yang, G. M.; Hwang, S. W.; Son, S. J. *Appl. Phys. Lett.* **2001**, *78*, 3265−3267.